Journal of Zhejiang University-SCIENCE A (Applied Physics & Engineering)
ISSN 1673-565X (Print); ISSN 1862-1775 (Online)
www.jzus.zju.edu.cn; www.springerlink.com
E-mail: jzus@zju.edu.cn

Numerical and experimental investigation of damping in a dam-break problem with fluid-structure interaction

Abdullah DEMIR[†1], Ali Ersin DINCER[2], Zafer BOZKUS[3], Arris S. TIJSSELING[4]

[1]*Structural Laboratory, Department of Civil Engineering, Erzurum Technical University, Yakutiye/Erzurum 25050, Turkey*

[2]*Hydromechanics Laboratory, Department of Civil Engineering, Erzurum Technical University, Yakutiye/Erzurum 25050, Turkey*

[3]*Hydromechanics Laboratory, Department of Civil Engineering, Middle East Technical University, Çankaya/Ankara 06800, Turkey*

[4]*Department of Mathematics and Computer Science, Eindhoven University of Technology, 5600 MB Eindhoven, The Netherlands*

[†]E-mail: abdullah.demir@erzurum.edu.tr

Received Sept. 13, 2018; Revision accepted Feb. 19, 2019; Crosschecked Feb. 27, 2019

Abstract: There have been few experimental and numerical studies on damping effects in fluid-structure interaction (FSI) problems. Therefore, a comprehensive experimental study was conducted to investigate such effects. In experiments, a water column in a container was released and hit a rubber plate. It continued its motion until hitting a downstream wall where pressure transducers had been placed. The experiments were repeated using rubber plates with different thickness and material properties. Free-surface profiles, displacements of the rubber plates, and pressures were recorded. In addition, a numerical model was developed to simulate the violent interaction between the fluid and the elastic structure. Smoothed particle hydrodynamics (SPH) and finite element method (FEM) were used to model the fluid and the structure. Contact mechanics was used to model the coupling mechanism. The obtained numerical results were in agreement with the experimental data. We found that damping is a less important parameter in the FSI problem considered.

Key words: Damping; Fluid-structure interaction (FSI); Smoothed particle hydrodynamics (SPH); Contact mechanics; Dam-break

https://doi.org/10.1631/jzus.A1800520 **CLC number:** TV312

1 Introduction

Many violent fluid-structure interaction (FSI) problems involve non-negligible two-way coupling effects, and different techniques have been proposed to model these FSI problems numerically. Among the numerical methods based on a Eulerian framework, finite difference (Forsythe and Wasow, 1960) and finite volume (Versteeg and Malalasekera, 1995) are the most popular. Also popular is the arbitrary Lagrangian Eulerian method (Amsden and Hirt, 1973) in which Eulerian approaches are used for fluid mediums and Lagrangian approaches for the structure. These Eulerian methods are time-consuming because re-meshing is often necessary. Pure Lagrangian methods may be more attractive for use in FSI problems involving large deformations, moving interfaces, and complex geometries. In recent years, finite element method (FEM) has been coupled with smoothed particle hydrodynamics (SPH) to simulate FSI problems (de Vuyst et al., 2005; Fourey et al., 2010, 2017; Groenenboom and Cartwright, 2010; Yang et al., 2012; Long et al., 2017).

SPH is a mesh-free Lagrangian technique in which the material is replaced by a set of particles to obtain numerical solutions. It was originally developed to simulate astrophysical problems (Gingold and Monaghan, 1977; Lucy, 1977) and was then applied

ORCID: Abdullah DEMIR, https://orcid.org/0000-0002-6392-648X

to fluid dynamics problems (Monaghan, 1994). Over recent decades, SPH has successfully been applied to different engineering problems in various fields (Dinçer, 2017; Dinçer et al., 2018).

FEM is an established numerical method used for structural analysis problems. It can be used to simulate fluids, but then re-meshing is necessary. Therefore, FEM is prevalent in the solution of structural vibrations where the displacements are small compared with those in fluid flows. It was used here for the solution of the structural part of the problem.

SPH-FEM was first proposed to investigate structure-structure impact problems using master-slave algorithms in which the penetration of SPH particles into finite-element meshes is prevented via calculated contact forces (Attaway et al., 1994). Master-slave algorithms are also used in FSI problems involving SPH-FEM (Groenenboom and Cartwright, 2010; Zhang et al., 2011). In these previous studies, the contact force was treated as a contact potential (de Vuyst et al., 2005; Yang et al., 2012). In some studies, finite element nodes are regarded as SPH particles (Fernandez-Mendez et al., 2005; Zhang et al., 2011). Fourey et al. (2017) studied the robustness of SPH-FEM coupling. They carried out a predictive-corrective solution strategy by determining forces from SPH and applying them to the finite element nodes, and then transferring revised coordinates from finite element nodes to SPH. In an earlier study, Fourey et al. (2010) studied the violent FSIs. The searching algorithm was a time-consuming routine for contact problems. Hu et al. (2014) focused on this topic and proposed a novel searching algorithm method. Different SPH improvements have been made, and coupling with FEM has been implemented. Long et al. (2016) implemented the FEM-ISPH (incompressible SPH) and FEM-WCSPH (weakly compressible SPH) for solving FSI problems.

The present study focuses on the dynamic analysis of the structure in a specific FSI problem, using SPH-FEM. A comprehensive dynamic analysis was performed, which included damping effects. The structure and fluid domains were solved together using a newly developed computer code. There are no available benchmark problems in which FSI is studied together with the damping properties of the structure. Therefore, in the present study, three novel experiments were conducted that can be used as benchmark problems. A thorough dynamic analysis of the elastic structure is presented. This is the first time that pressures have been recorded in an FSI dam-break experiment containing a highly deformable rubber plate. In addition, the fluid hits both faces of the structure at different times in a single experiment.

2 Numerical model

2.1 SPH

As a Lagrangian particle approach, SPH is used to calculate field variables by transforming partial differential equations into ordinary differential equations with the help of kernel functions. It has superiority over mesh-based methods for handling problems involving complex geometries, large deformations, and free surfaces.

The Euler equations of fluid dynamics in discrete SPH form can be stated as (Monaghan, 1989, 1994; Liu and Liu, 2003):

$$\frac{\mathrm{d}\rho_i}{\mathrm{d}t}=\sum_{j=1}^{N}m_j\boldsymbol{V}_{ij}\cdot\nabla W_{ij}, \tag{1}$$

$$\frac{\mathrm{d}\boldsymbol{V}_i}{\mathrm{d}t}=\sum_{j=1}^{N}\left(\frac{P_i}{\rho_i^2}+\frac{P_j}{\rho_j^2}+\pi_{ij}\right)\nabla W_{ij}+\boldsymbol{f}_\mathrm{b}+\Delta\boldsymbol{\lambda}, \tag{2}$$

$$P=P_0\left[\left(\frac{\rho}{\rho_0}\right)^7-1\right], \tag{3}$$

$$\frac{\mathrm{d}\boldsymbol{r}_i}{\mathrm{d}t}=\boldsymbol{V}_i+0.05\sum_{j=1}^{N}m_j\left(\frac{\boldsymbol{V}_{ij}}{\rho_i}\right)W_{ij}, \tag{4}$$

where subscripts i and j denote different neighbor particles, m is the mass, ρ is the density, ρ_0 is the initial density, t is the time, $\boldsymbol{V}$ is the velocity vector and $\boldsymbol{V}_{ij}=\boldsymbol{V}_i-\boldsymbol{V}_j$, P is the pressure, P_0 is the initial pressure assigned as hydrostatic pressure to all N particles, $\boldsymbol{f}_\mathrm{b}$ is the body force including gravity, $\Delta\boldsymbol{\lambda}$ is the contact force applied by the structure, as explained in the following part, $W_{ij}=W(|\boldsymbol{r}_{ij}|,h)$ is the

cubic spline kernel, ∇W_{ij} is its gradient, h is the smoothing length taken as 1.33 times the initial particle spacing, and $\boldsymbol{r}$ is the position vector and $\boldsymbol{r}_{ij}=\boldsymbol{r}_i-\boldsymbol{r}_j$. The last term in Eq. (4) was added for the stability.

In Eq. (2), π_{ij} is the artificial viscosity, used to stabilize the numerical algorithm and mimic the physical viscosity (Monaghan, 1992):

$$\pi_{ij}=\frac{-\phi\mu_{ij}\bar{c}_{ij}+\varphi\mu_{ij}^2}{\bar{\rho}_{ij}}, \tag{5}$$

where ϕ and φ are empirical coefficients, taken as 1 and 0.2, respectively.

$$\bar{c}_{ij}=\frac{c_i+c_j}{2},\quad \bar{\rho}_{ij}=\frac{\rho_i+\rho_j}{2}, \tag{6}$$

$$\mu_{ij}=\frac{h\boldsymbol{V}_{ij}\cdot\boldsymbol{r}_{ij}}{\boldsymbol{r}_{ij}^2+0.001h^2}, \tag{7}$$

where c is an artificial sound speed, usually taken as much lower than the actual speed to limit central processing unit (CPU) time. The leap-frog algorithm is used for time marching and the maximum time step is calculated from the Courant-Friedrichs-Lewy (CFL) condition (Hirsch, 1988; Anderson, 1995). The mirror particle method is used to impose a free-slip boundary condition on the fixed walls where FSI is not important. The boundary between an elastic structure and the fluid is imposed with SPH-FEM, as explained below.

2.2 FEM

FEM is used to solve the structural part of the FSI problem. A dynamic method, in which stiffness and mass matrices of SPH particles and FEM meshes are solved by the Wilson-θ method, is applied to FSI problems using Rayleigh damping. The Wilson-θ method (Wilson et al., 1973) is unconditionally stable, and is used for time integration. An extended time step is used to make the method more stable. Structural motion in one time step, Δt, is extended to $\theta\Delta t$, where θ is a time extension factor greater than 1. Chopra (2007) stated that 1.42 is an optimum value for θ.

Corresponding incremental responses are defined for γ=1/2 and β=1/6, which are established time integration parameters (Newmark, 1959). Replacing $\theta\Delta t$ by δt and incremental responses by $\delta\boldsymbol{u}$, $\delta\dot{\boldsymbol{u}}$, and $\delta\ddot{\boldsymbol{u}}$ gives the corresponding equations of motion for the extended time step:

$${}^t\delta\ddot{\boldsymbol{u}}=\frac{6}{(\delta t)^2}{}^t\delta\boldsymbol{u}-\frac{6}{\delta t}{}^t\dot{\boldsymbol{u}}-3{}^t\ddot{\boldsymbol{u}}, \tag{8}$$

$${}^t\delta\dot{\boldsymbol{u}}=\frac{3}{\delta t}{}^t\delta\boldsymbol{u}-3{}^t\dot{\boldsymbol{u}}-\frac{\delta t}{2}{}^t\ddot{\boldsymbol{u}}, \tag{9}$$

where ${}^t\dot{\boldsymbol{u}}$ and ${}^t\ddot{\boldsymbol{u}}$ are the velocity and acceleration, respectively, at time t.

Thus, the well-known equation of motion is discretized as

$${}^t\boldsymbol{M}{}^t\delta\ddot{\boldsymbol{u}}+{}^t\boldsymbol{C}{}^t\delta\dot{\boldsymbol{u}}+{}^t\boldsymbol{K}{}^t\delta\boldsymbol{u}={}^t\delta\boldsymbol{F}, \tag{10}$$

where ${}^t\boldsymbol{M}$, ${}^t\boldsymbol{C}$, ${}^t\boldsymbol{K}$ are mass, damping, and stiffness matrices, respectively, at time t, and ${}^t\delta\boldsymbol{F}$ is the incremental force vector for the extended time step.

This equation of motion is redefined by substituting Eqs. (8) and (9) into Eq. (10):

$${}^t\hat{\boldsymbol{K}}{}^t\delta\boldsymbol{u}={}^t\delta\hat{\boldsymbol{F}}, \tag{11}$$

where ${}^t\hat{\boldsymbol{K}}$ is the effective stiffness matrix and $\hat{\boldsymbol{F}}$ is the effective external force. Solving Eq. (11) gives the incremental displacement ${}^t\delta\boldsymbol{u}$ for the extended time step. The incremental velocity ${}^t\delta\dot{\boldsymbol{u}}$ and acceleration ${}^t\delta\ddot{\boldsymbol{u}}$ for the extended time step are calculated from Eqs. (8) and (9), respectively.

Damping has a role in the motion of structures and is included in Eqs. (10) and (11). Rayleigh damping is used, which means that the damping matrix is related to the mass matrix and the stiffness matrix:

$$\boldsymbol{C}=\alpha_0\boldsymbol{M}+\alpha_1\boldsymbol{K}, \tag{12}$$

where α_0 and α_1 are constants.

Rayleigh constants are determined from specified damping ratios ζ_i and ζ_j of the ith and jth modes of vibration, respectively. The relation is given by Chopra (2007) as follows:

$$\frac{1}{2}\begin{bmatrix} \dfrac{1}{\omega_i} & \omega_i \\ \dfrac{1}{\omega_j} & \omega_j \end{bmatrix}\begin{bmatrix} \alpha_0 \\ \alpha_1 \end{bmatrix}=\begin{bmatrix} \zeta_i \\ \zeta_j \end{bmatrix}, \tag{13}$$

where ω_i and ω_j are the natural frequencies for the ith and jth modes.

If both modes are assumed to have the same damping ratio ζ, the Rayleigh constants are:

$$\alpha_0=\zeta\frac{2\omega_i\omega_j}{\omega_i+\omega_j}, \tag{14a}$$

$$\alpha_1=\zeta\frac{2}{\omega_i+\omega_j}. \tag{14b}$$

A detailed determination of the natural frequencies of structures is described by Blevins (2016).

3 Numerical model

The coupling mechanism is satisfied using contact mechanics (Demir, 2017). Contact mechanics is based on taking intersecting domains apart from each other. This is done by applying the contact forces to the intersecting domains. The potential of contact forces is determined and added to the total potential of the system. The contact forces and the corresponding displacements are calculated by solving the governing equations of the system derived from its total potential.

The geometry of contact is illustrated by a contact particle and a target surface (Fig. 1). In this illustration, the target surface is defined with one finite line, which can be the surface of any finite element. ${}^{t+\delta t}\boldsymbol{P}_A^{(i-1)}$, ${}^{t+\delta t}\boldsymbol{P}_B^{(i-1)}$, ${}^{t+\delta t}\boldsymbol{P}_C^{(i-1)}$, and ${}^{t+\delta t}\boldsymbol{P}_p^{(i-1)}$ are position vectors of node A, node B, point C, and particle p, respectively, at time $t+\delta t$ and the $(i-1)$th iteration. At that time, the overlap of a particle is defined as $\boldsymbol{O}_p^{(i-1)}$.

Nodes A and B are the nodal coordinates of the target line, and C is the projection of water particle p on the target line. The location of point C, which is the contact point, is defined from node A as ξl, where l is the length of the target line and ξ is a parameter indicating the location of point C. The contact force applied to the water particle is defined as ${}^{t+\delta t}\boldsymbol{\lambda}_p^{(i-1)}$, and is applied to the target surface. SPH defines the motion of the water particle from time t to time $(t+\delta t)$ and contact mechanics takes away the water particle from the structural domain from time $(t+\delta t)$ to time $(t+\Delta t)$. This time period $(\Delta t-\delta t)$ is called the pseudo time interval.

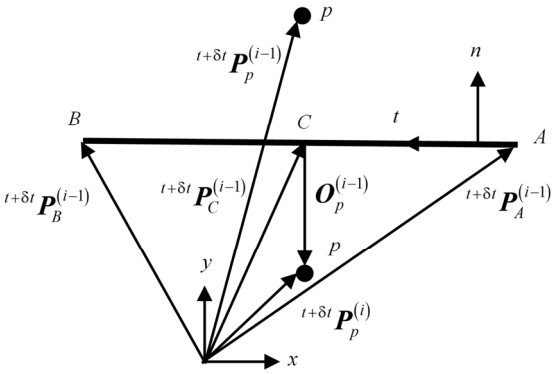

Fig. 1 Configuration of a simple contact with fluid at the top and solid at the bottom

Parameter ξ is defined by

$$\begin{aligned}\xi&=\frac{\boldsymbol{n}^{\mathrm{T}}}{l}\left({}^{t+\delta t}\boldsymbol{P}_C^{(i-1)}-{}^{t+\delta t}\boldsymbol{P}_A^{(i-1)}\right)\\&=\frac{\boldsymbol{n}^{\mathrm{T}}}{l}\left[\left({}^{t+\delta t}\boldsymbol{P}_p^{(i-1)}-\boldsymbol{O}_p^{(i-1)}\right)-{}^{t+\delta t}\boldsymbol{P}_A^{(i-1)}\right],\end{aligned} \tag{15}$$

where $\boldsymbol{n}$ is the local normal unit vector.

Reactional forces at nodes A and B can be written as

$${}^{t+\delta t}\boldsymbol{\lambda}_A^{(i-1)}=-\left(1-\xi\right){}^{t+\delta t}\boldsymbol{\lambda}_p^{(i-1)}, \tag{16}$$

$${}^{t+\delta t}\boldsymbol{\lambda}_B^{(i-1)}=-\xi\,{}^{t+\delta t}\boldsymbol{\lambda}_p^{(i-1)}. \tag{17}$$

Accordingly, the corresponding potential is

$$\begin{aligned}\Pi_p=&\left({}^{t+\delta t}\boldsymbol{\lambda}_p^{(i)}\right)^{\mathrm{T}}\left(\Delta\boldsymbol{u}_p^{(i)}+\boldsymbol{O}_p^{(i-1)}\right)\\&+\left({}^{t+\delta t}\boldsymbol{\lambda}_A^{(i)}\right)^{\mathrm{T}}\Delta\boldsymbol{u}_A^{(i)}+\left({}^{t+\delta t}\boldsymbol{\lambda}_B^{(i)}\right)^{\mathrm{T}}\Delta\boldsymbol{u}_B^{(i)},\end{aligned} \tag{18}$$

where $\Delta\boldsymbol{u}_A^{(i)}$, $\Delta\boldsymbol{u}_B^{(i)}$, and $\Delta\boldsymbol{u}_p^{(i)}$ are the incremental displacements at node A, node B, and particle p, respectively.

Substituting Eqs. (16) and (17) into Eq. (18),

$$\begin{aligned}\Pi_p=&\left({}^{t+\delta t}\boldsymbol{\lambda}_p^{(i)}\right)^{\mathrm{T}}\left(\Delta\boldsymbol{u}_p^{(i)}+\boldsymbol{O}_p^{(i-1)}\right)\\&+\left[-(1-\xi)\,{}^{t+\delta t}\boldsymbol{\lambda}_p^{(i)}\right]^{\mathrm{T}}\Delta\boldsymbol{u}_A^{(i)}\\&+\left(-\xi\,{}^{t+\delta t}\boldsymbol{\lambda}_p^{(i)}\right)^{\mathrm{T}}\Delta\boldsymbol{u}_B^{(i)}.\end{aligned}\tag{19}$$

The new ${}^{t+\delta t}\boldsymbol{\lambda}_p^{(i)}$ is defined as

$${}^{t+\delta t}\boldsymbol{\lambda}_p^{(i)}={}^{t+\delta t}\boldsymbol{\lambda}_p^{(i-1)}+\Delta\boldsymbol{\lambda}_p^{(i)}.\tag{20}$$

Substituting Eq. (20) into Eq. (19) gives the potential of the contact forces, which was derived by Bathe and Chaudhary (1985) for structural problems:

$$\begin{aligned}\Pi_p=&\left({}^{t+\delta t}\boldsymbol{\lambda}_p^{(i-1)}+\Delta\boldsymbol{\lambda}_p^{(i)}\right)^{\mathrm{T}}\\&\left[\left(\Delta\boldsymbol{u}_p^{(i)}+\boldsymbol{O}_p^{(i-1)}\right)-(1-\xi)\Delta\boldsymbol{u}_A^{(i)}-\xi\Delta\boldsymbol{u}_B^{(i)}\right].\end{aligned}\tag{21}$$

The matrix form of the defined potential of contact forces with added mass participation is

$$\begin{aligned}&\begin{bmatrix}{}^{t+\Delta t}\boldsymbol{K}_{\mathrm{solid}}^{(i-1)} & \boldsymbol{0} & \left[{}^{t+\Delta t}\boldsymbol{K}_{\mathrm{c}}^{(i-1)}\right]\\ \boldsymbol{0} & \dfrac{2}{(\Delta t)^2}\,{}^{t+\Delta t}\boldsymbol{M}_p^{(i-1)} & \\ \left[{}^{t+\Delta t}\boldsymbol{K}_{\mathrm{c}}^{(i-1)}\right]^{\mathrm{T}} & \boldsymbol{0} & \end{bmatrix}\begin{bmatrix}\Delta\boldsymbol{u}^{(i)}\\ \Delta\boldsymbol{\lambda}^{(i)}\end{bmatrix}\\&=\begin{bmatrix}{}^{t+\Delta t}\boldsymbol{R}\\ \boldsymbol{0}\end{bmatrix}-\begin{bmatrix}{}^{t+\Delta t}\boldsymbol{F}^{(i-1)}\\ \boldsymbol{0}\end{bmatrix}+\begin{bmatrix}{}^{t+\Delta t}\boldsymbol{R}_{\mathrm{c}}^{(i-1)}\\ {}^{t+\Delta t}\boldsymbol{O}_{\mathrm{c}}^{(i-1)}\end{bmatrix},\end{aligned}\tag{22}$$

where ${}^{t+\Delta t}\boldsymbol{K}_{\mathrm{solid}}^{(i-1)}$ is the tangential stiffness matrix of the structure, ${}^{t+\Delta t}\boldsymbol{K}_{\mathrm{c}}^{(i-1)}$ is the contact stiffness matrix, ${}^{t+\Delta t}\boldsymbol{M}_p^{(i-1)}$ is the mass matrix of fluid particles, $\Delta\boldsymbol{u}^{(i)}$ is the incremental displacement vector, $\Delta\boldsymbol{\lambda}^{(i)}$ is the incremental contact forces vector, ${}^{t+\Delta t}\boldsymbol{R}$ is the total applied external loads vector, ${}^{t+\Delta t}\boldsymbol{F}^{(i-1)}$ is the equivalent nodal forces vector, ${}^{t+\Delta t}\boldsymbol{R}_{\mathrm{c}}^{(i-1)}$ is the contact forces vector for solid, and ${}^{t+\Delta t}\boldsymbol{O}_{\mathrm{c}}^{(i-1)}$ is the overlaps vector. Addition of the mass matrix of SPH particles to Eq. (22) will give the desired unified equation of motion for both domains.

The contact force between SPH particles and the structure $\Delta\boldsymbol{\lambda}^{(i)}$, the displacement of the structure $\Delta\boldsymbol{u}_{\mathrm{solid}}^{(i)}$, and the displacement of the fluid particles $\Delta\boldsymbol{u}_p^{(i)}$ are determined from Eq. (22). Calculated contact forces and displacements $\Delta\boldsymbol{u}_{\mathrm{solid}}^{(i)}$ are applied to the structure directly. In contrast, displacements $\Delta\boldsymbol{u}_p^{(i)}$ are not applied to SPH particles so as not to violate the continuity of the SPH method. Instead, contact forces $\Delta\boldsymbol{\lambda}^{(i)}$ are applied to the invading SPH particles as external boundary forces.

4 Experimental setup

A series of experiments was carried out to investigate the structural damping effect. The setup was similar to the one used by Koshizuka et al. (1995). The main improvement of this experimental setup was that the pressures at the downstream wall were recorded. Experiments were carried out using rubber plates with different material and geometric properties. In addition, complete water surface profiles and tip displacements of rubber plates were provided. Fig. 2 is a 2D illustration and Fig. 3 a photograph of the experimental setup.

A rubber plate was fixed in the middle of the bottom of the container. A water column was placed at the left of the container. A leak-proof knife gate was used to quickly release the water column. The motion of the knife gate was started by releasing an 8 kg weight tied to the gate by a steel rope. The average velocity of the knife gate was measured as 2.5 m/s and the corresponding lift time was 0.12 s. According to Lauber and Hager (1998), this gate opening can be considered as instantaneous since the lift time was less than $\sqrt{2H_0/g}=0.8\,\mathrm{s}$, where H_0 is the height of the water column and g is the gravitational acceleration.

Released water hit the rubber plate and found its way towards the downstream wall of the container, which was assumed to be fixed and rigid. To capture the location and magnitude of the peak pressure, transducers were placed every 2 cm on the downstream wall (Fig. 2). Data recording for the transducers was activated by the movement of an

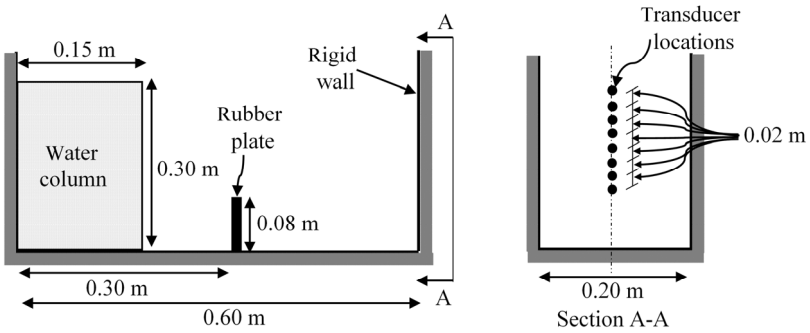

Fig. 2 A 2D illustration of the experimental setup

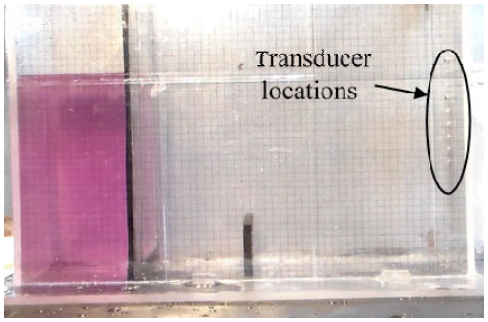

Fig. 3 Photograph of the experimental setup

Table 1 Properties of the rubber plates

Thickness (mm)	Modulus of elasticity (MPa)	Density (kg/m^3)	Damping ratio (%)
5	20	1250	25
10	5	1300	12
15	14	1275	37

Fig. 4 Tensile testing of rubbers

accelerometer located on the knife gate. Dynamic pressure transducers with built-in unity gain voltage amplifiers were used. These units were selected because of their high resonant frequency and acceleration-compensated quartz element, and because their signal quality is almost independent of the cable length and motion. The calibration procedure as supplied by the manufacturer was in compliance with ISO 10012-1 (ISO, 1992) and the former MIL-STD-45662A. The sampling rate was 1000 Hz.

Three different rubber plates were used to investigate the damping effect. Each plate had a different thickness, modulus of elasticity, and damping ratio (Table 1). The modulus of elasticity of the rubbers was determined using a tensile testing machine (Fig. 4). Acquired data were linearized (Table 1).

The damping ratios of the rubber plates were determined experimentally. In brief, in the experiments, each rubber plate was fixed at its bottom as in the main setup. A known displacement, consistent with the maximum displacements in the main experiment, was applied to the rubbers. Energy dissipation was calculated from the oscillation of the rubber plates using

$$\zeta = \eta \Big/ \sqrt{4\pi^2 + \eta^2}\,, \tag{23}$$

where $\eta=\ln(x_0/x_1)$, x_0 is the first peak displacement, and x_1 is the second peak displacement. These variables were read from Fig. 5 which shows the oscillations of the rubber plates after an initial displacement.

In this study, our aim was to investigate the damping effect. Therefore, two numerical analyses were carried out for each rubber plate. The first analysis included the real damping coefficient and

the second was the no damping case. Thus, the effect of damping could be observed for each rubber plate.

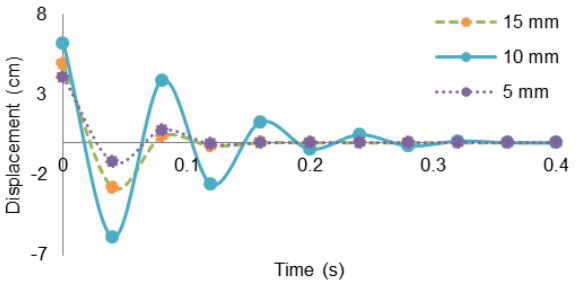

Fig. 5 Experimental oscillations of the rubber plates of different thickness

5 Numerical setup

Simulations of the experiments were obtained using a computer tool developed according to the proposed numerical models. The fluid domain was simulated with SPH and the structure domain with FEM. The interaction between the fluid and the structure was modelled by contact mechanics. A total of 20 000 SPH particles were used to represent the water column. Sixty finite elements were used for the 5-mm rubber plates, and 120 for both the 10-mm and 15-mm plates. Dividing the thickness of the plate into 4 and the height into 30, gave 120 elements. The walls of the container were simulated using the

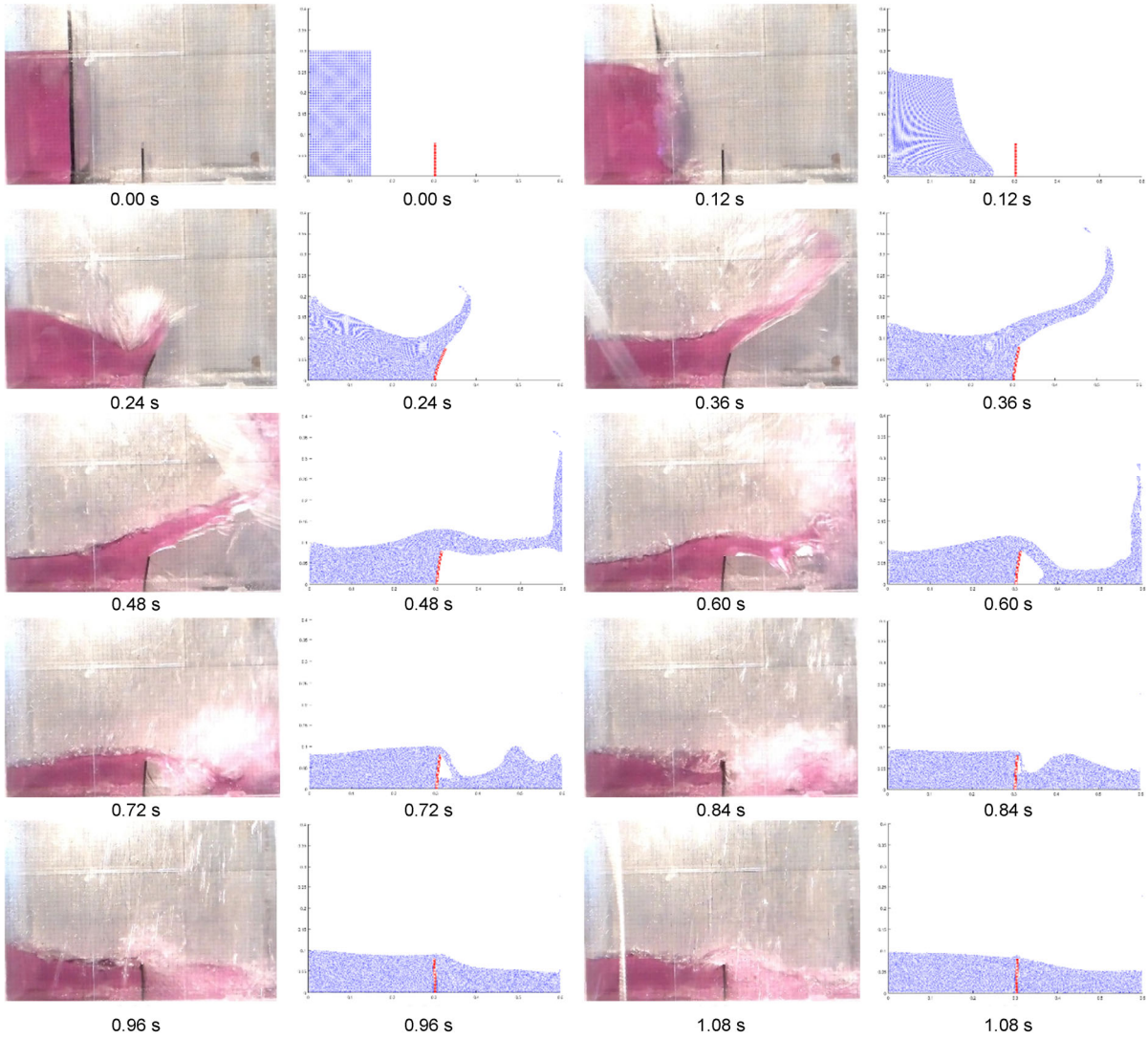

Fig. 6 Free-surface profiles of experiment with 5-mm rubber plate together with the numerical results

mirror particle method with a free-slip boundary condition.

In the simulations, the length of the time step was taken as 2.10^{-5} s for both the fluid and the structure. In addition, the time step extension constant θ was taken as 1.42 (Chopra, 2007). The modulus of elasticity of the rubber was taken as constant throughout the simulation, because it was assumed to be within the elastic range during the experiments. Although material nonlinearity was not taken into account, geometric nonlinearity was considered. In the theory of Rayleigh, the damping ratios for two different modes of vibration are assumed to be the same for the calculation of the constants α_0 and α_1.

6 Results and validation

A set of experiments was carried out for different rubber plates using the experimental setup defined above. The free-surface profiles of water, displacements of rubber, and pressures recorded on the right wall of the container are presented. The free-surface profiles and displacements of rubber were recorded by a high-definition camera supporting 25 frames per second.

6.1 Free-surfaces

Free-surface profiles are shown for each set of experiments for 5-mm, 10-mm, and 15-mm rubber plates in Figs. 6, 7, and 8, respectively, together with

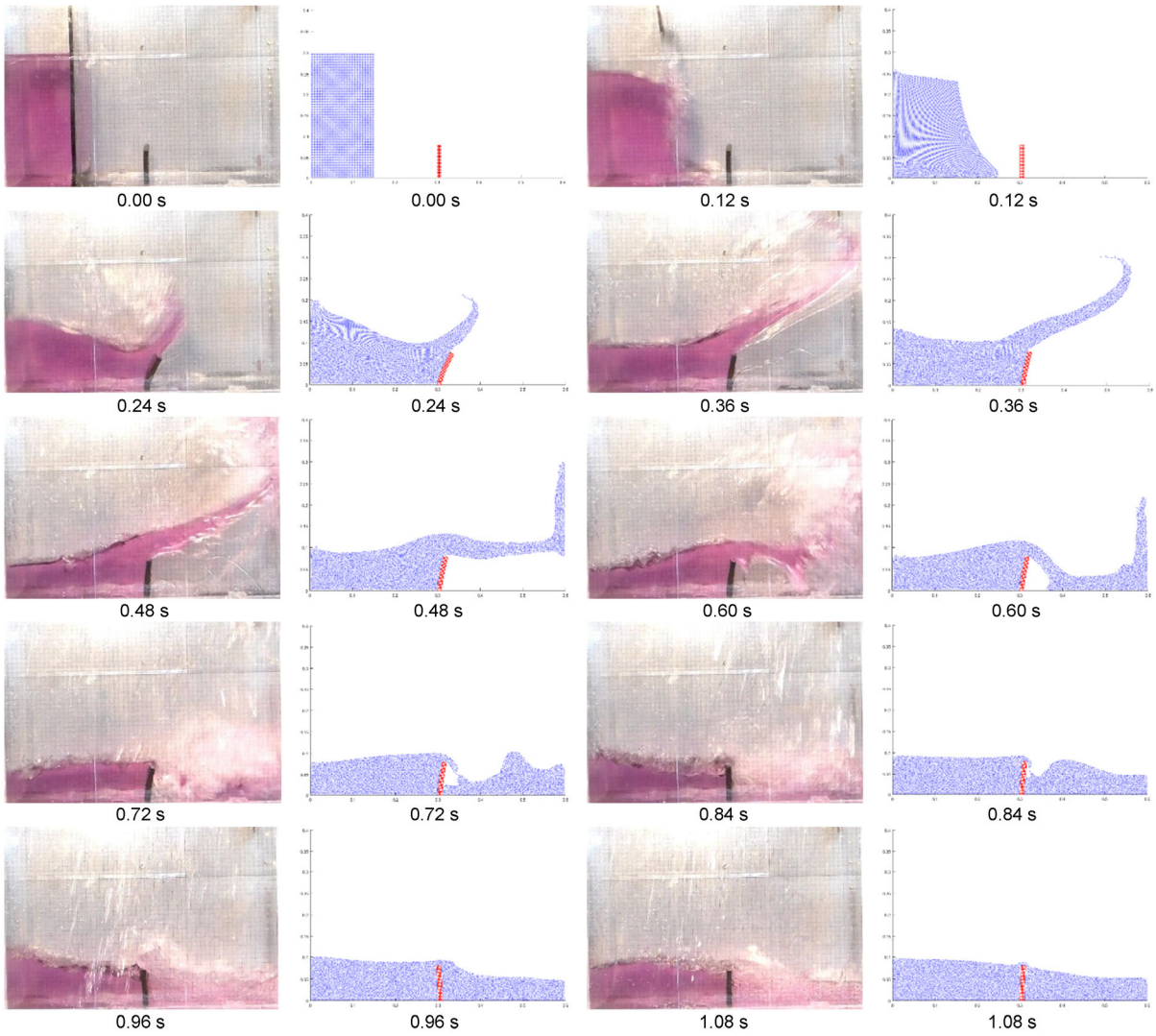

Fig. 7 Free-surface profiles of the experiment with a 10-mm rubber plate together with the numerical results

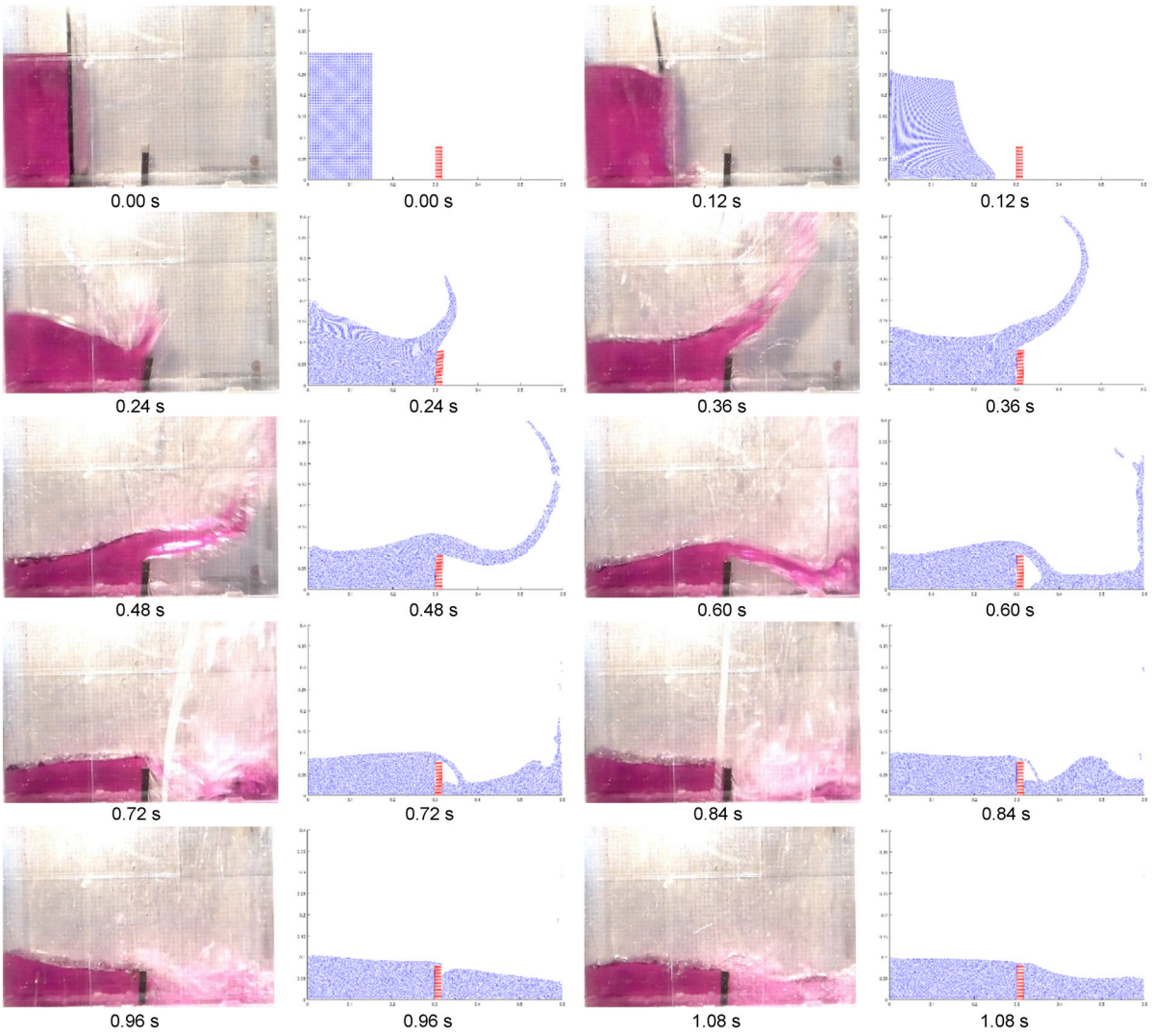

Fig. 8 Free-surface profiles of the experiment with a 15-mm rubber plate together with the numerical results

the numerical results. Calculated and measured free surfaces show good agreement in view of the violence of the flow.

6.2 Displacement of rubber plate

Tip displacements of the rubber plates with thickness of 5 mm, 10 mm, and 15 mm are given in Figs. 9, 10, and 11, respectively. In addition, simulation results for the actual damping coefficient and zero damping coefficient are presented to reveal the damping effect.

Experiments were carried out in 3D and simulated in 2D. Although it was assumed that the geometric and flow properties were uniform through the width of the water tank (0.2 m), there were some inevitable irregularities. These irregularities resulted in differences in pressure distributions on the rubber plate across its width. Therefore, additional oscillations were observed in the experiment.

Although measured and simulated peak tip displacements were similar, the times of occurrence were different. This was mainly because of the upward motion of the knife gate, even though the motion was considered instantaneous according to Lauber and Hager (1998).

Although damping had an effect on the structural analysis, the current experimental and numerical results show that its effect was not significant in this

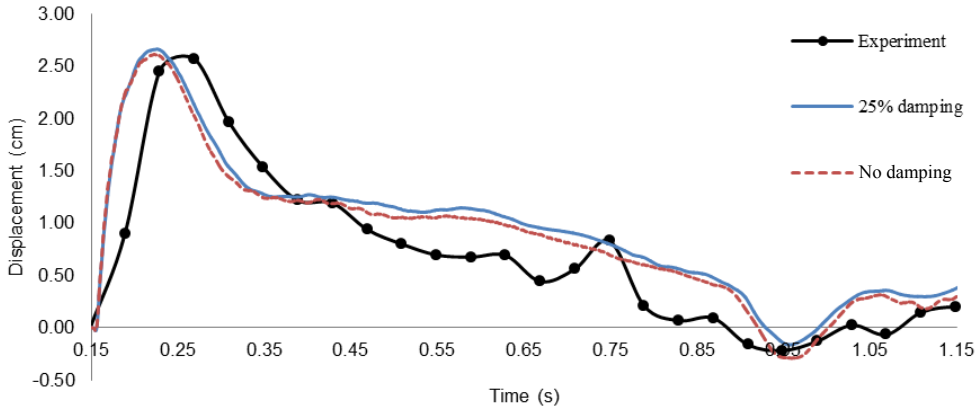

Fig. 9 Tip displacements of the 5-mm rubber plate

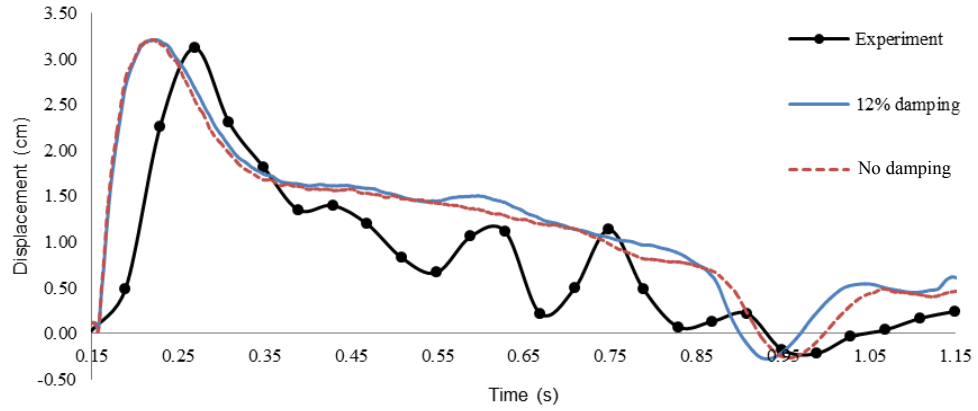

Fig. 10 Tip displacements of the 10-mm rubber plate

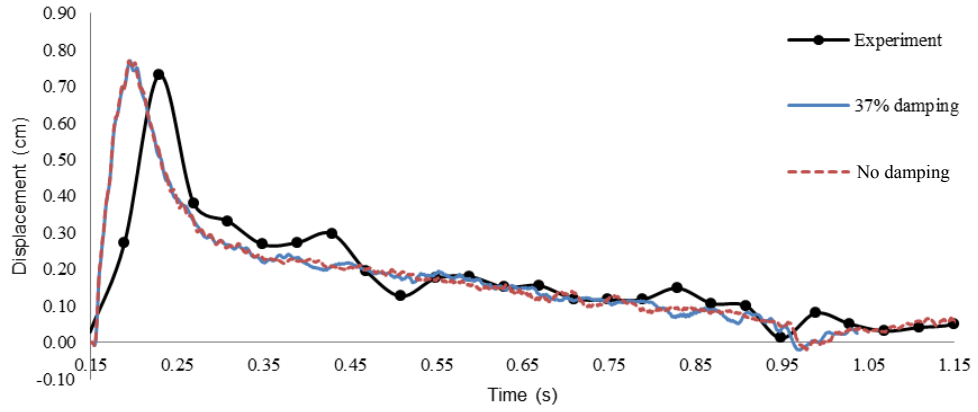

Fig. 11 Tip displacements of the 15-mm rubber plate

type of FSI problem. To illustrate its effect on structural mechanics, a constant 50 N force was suddenly applied to the tip of the 10-mm rubber plate. Corresponding tip displacements for the real damping coefficient and no damping are given in Fig. 12. Damping affected the behavior of the structure significantly. A damped motion always has smaller displacements than undamped motion in the case of constant force. The reason is the transfer of energy to the rubber plate. The energy transferred to the 10-mm

rubber plate by a constant 50 N force is given in Fig. 13. The energy transferred to the undamped rubber plate was more than that transferred to the damped plate. It is also obvious from Fig. 12 that the undamped structure had a higher displacement.

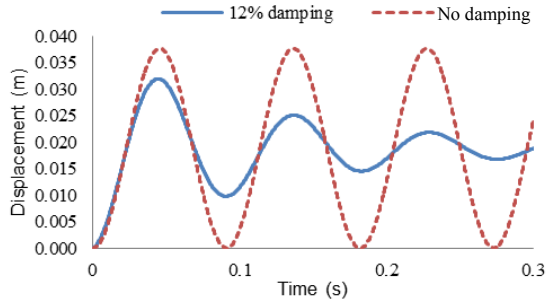

Fig. 12 Tip displacements of the 10-mm rubber plate under a suddenly applied constant 50 N force

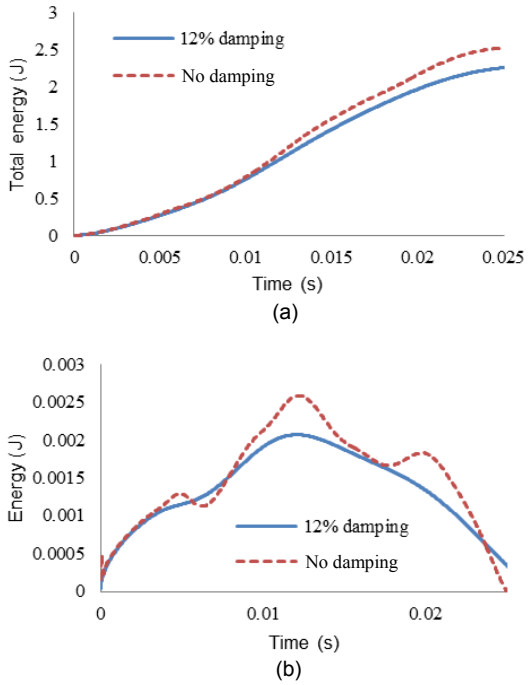

Fig. 13 Total energy (a) and energy transferred to the plate in a single time step (b) in the 10-mm rubber plate, due to a suddenly applied constant force of 50 N

In contrast to the results with the constant force, tip displacements were slightly greater or the same for damped and undamped cases in the FSI problem. The reason is that the force is not foreknown, but generated by the continuous interaction between the fluid and the structure. The time history of energy transfer to the structure from the fluid is given in Fig. 14. If the total energies (from the beginning to maximum tip displacement) of undamped and damped cases for each rubber plate are compared, it can be seen that slightly more energy is transferred in the damped case. This can be explained by the concept of energy dissipation. Energy dissipation is related to the rigidity of the dissipater. When the dissipater/structure is more rigid, more energy is dissipated. A structure behaves more rigidly by including the damping term in Eq. (10). Therefore, energy dissipation, most of which is the energy transferred to the structure, is higher for the damped case.

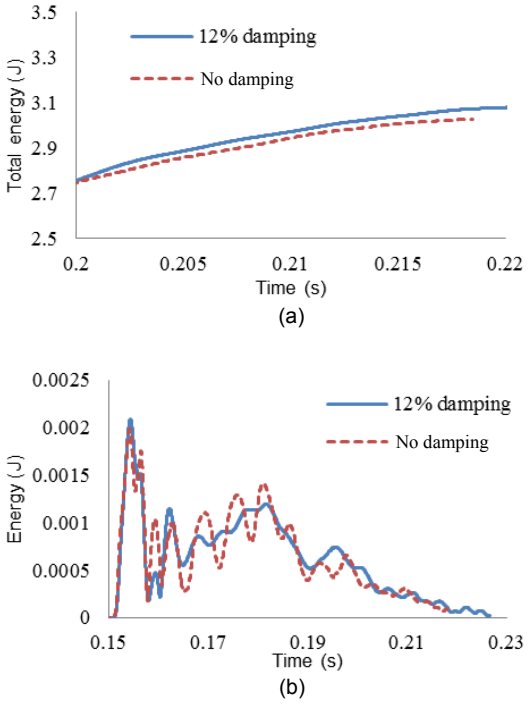

Fig. 14 Total energy (a) and energy transferred to the plate in a single time step (b) in the 10-mm rubber plate during the FSI experiment

Thus, almost the same tip displacements are achieved.

6.3 Pressures

Peak pressures and their locations on the right rigid wall are given in Table 2 for each rubber plate. The pressure histories (Figs. 15–17) show that water

hit the right rigid wall slightly earlier in the numerical simulations. Otherwise, the calculated pressures were in good agreement with the measured ones.

Table 2 Peak pressures for each experiment

Rubber plate thickness (mm)	Location of transducer* (mm)	Peak pressure (kPa)	
		Measured	Calculated
5	32	15.2	14.2
10	28	16.1	15.7
15	32	12.0	11.3

* Distance between the transducer reading the peak pressure and the bottom wall

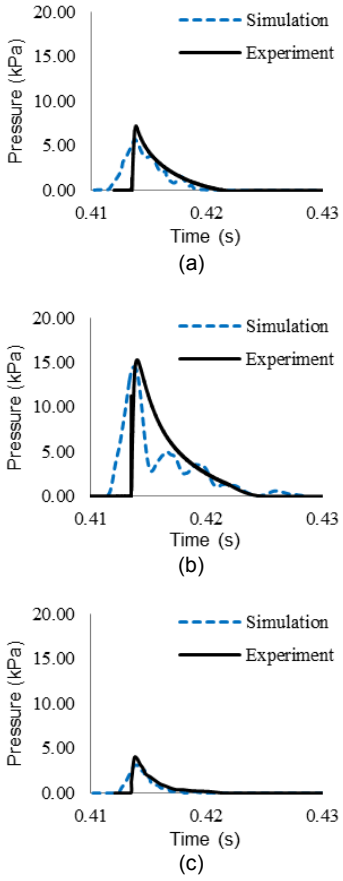

Fig. 15 Measured (solid line) and calculated (dashed line) pressure readings for the 5-mm rubber plate at 30 cm (a), 32 cm (b), and 34 cm (c) from the bottom wall

7 Conclusions

A series of experiments has been carried out to investigate the effects of damping in FSI problems.

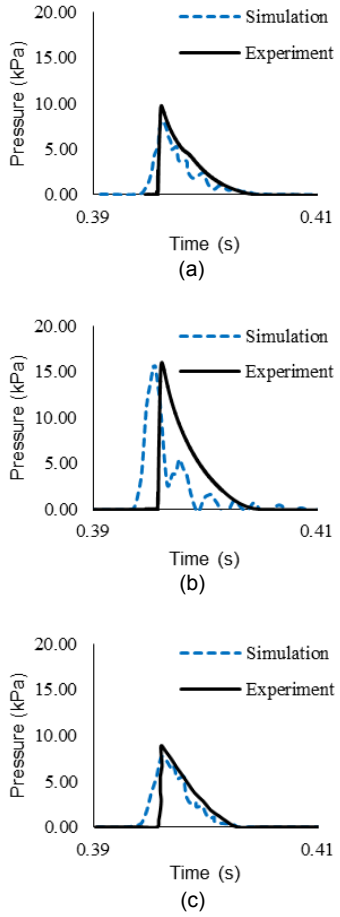

Fig. 16 Measured (solid line) and calculated (dashed line) pressure readings for the 10-mm rubber plate at 26 cm (a), 28 cm (b), and 30 cm (c) from the bottom wall

An SPH-FEM-based numerical model was developed in which contact mechanics is used for FSI coupling. Damping ratios of rubber plates were measured and used in the numerical model. This is the first time that impact pressures have been recorded in an FSI experiment containing a highly deformable rubber plate. Also, water hit both sides of the rubber plate at different times in a single experiment and the corresponding water flow and displacements of the rubber plate were presented.

The free-surface profiles, displacements of rubber plates, and pressures on the right wall of the container were successfully simulated with the SPH-FEM-based FSI model. The obtained results show that damping is not effective in this type of FSI problem and is not essential to be used in inertia-driven problems containing continuous interaction.

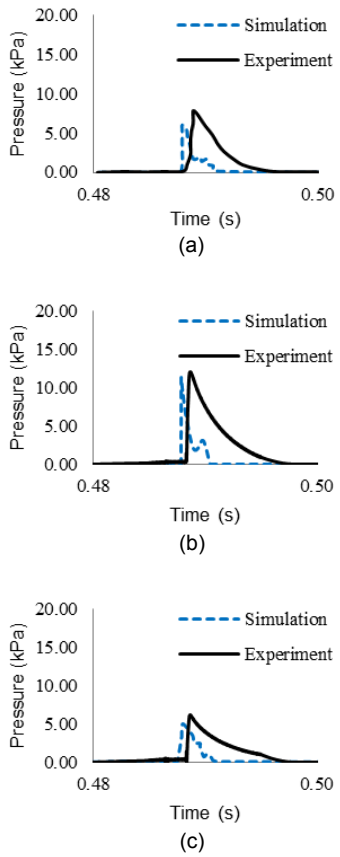

Fig. 17 Measured (solid line) and calculated (dashed line) pressure readings for the 15-mm rubber plate at 30 cm (a), 32 cm (b), and 34 cm (c) from the bottom wall

References

Amsden AA, Hirt CW, 1973. YAQUI: an Arbitrary Lagrangian-Eulerian Computer Program for Fluid Flow at All Speeds. Los Alamos Scientific Laboratory, New Mexico, USA.

Anderson JD, 1995. Computational Fluid Dynamics: the Basics with Applications. McGraw-Hill, New York, USA.

Attaway SW, Heinstein MW, Swegle JW, 1994. Coupling of smooth particle hydrodynamics with the finite element method. *Nuclear Engineering and Design*, 150(2-3):199-205. https://doi.org/10.1016/0029-5493(94)90136-8

Bathe KJ, Chaudhary A, 1985. A solution method for planar and axisymmetric contact problems. *International Journal for Numerical Methods in Engineering*, 21(1):65-88. https://doi.org/10.1002/nme.1620210107

Blevins RD, 2016. Formulas for Dynamics, Acoustics and Vibration. John Wiley & Sons, Chichester, West Sussex, UK.

Chopra AK, 2007. Dynamics of Structures: Theory and Applications to Earthquake Engineering. Pearson/Prentice Hall, Upper Saddle River, USA.

de Vuyst T, Vignjevic R, Campbell JC, 2005. Coupling between meshless and finite element methods. *International Journal of Impact Engineering*, 31(8):1054-1064. https://doi.org/10.1016/j.ijimpeng.2004.04.017

Demir A, 2017. Multi Segment Continuous Cables with Frictional Contact Along Their Span. PhD Thesis, Middle East Technical University, Ankara, Turkey.

Dinçer AE, 2017. Numerical Investigation of Free-surface and Pipe Flow Problems by Smoothed Particle Hydrodynamics. PhD Thesis, Middle East Technical University, Ankara, Turkey.

Dinçer AE, Bozkuş Z, Tijsseling AS, 2018. Prediction of pressure variation at an elbow subsequent to a liquid slug impact by using smoothed particle hydrodynamics. *Journal of Pressure Vessel Technology*, 140(3):031303. https://doi.org/10.1115/1.4039696

Fernandez-Mendez S, Bonet J, Huerta A, 2005. Continuous blending of SPH with finite elements. *Computers & Structures*, 83(17-18):1448-1458. https://doi.org/10.1016/j.compstruc.2004.10.019

Forsythe GE, Wasow WR, 1960. Finite-difference Methods for Partial Differential Equations. Wiley, New York, USA.

Fourey G, Oger G, Le Touzé D, et al., 2010. Violent fluid-structure interaction simulations using a coupled SPH/FEM method. *IOP Conference Series: Materials Science and Engineering*, 10(1):012041. https://doi.org/10.1088/1757-899x/10/1/012041

Fourey G, Hermange C, Le Touzé D, et al., 2017. An efficient FSI coupling strategy between smoothed particle hydrodynamics and finite element methods. *Computer Physics Communications*, 217:66-81. https://doi.org/10.1016/j.cpc.2017.04.005

Gingold RA, Monaghan JJ, 1977. Smoothed particle hydrodynamics: theory and application to non-spherical stars. *Monthly Notices of the Royal Astronomical Society*, 181(3):375-389. https://doi.org/10.1093/mnras/181.3.375

Groenenboom PHL, Cartwright BK, 2010. Hydrodynamics and fluid-structure interaction by coupled SPH-FE method. *Journal of Hydraulic Research*, 48(S1):61-73. https://doi.org/10.1080/00221686.2010.9641246

Hirsch C, 1988. Numerical Computation of Internal and External Flows. John Wiley & Sons, New York, USA.

Hu DA, Long T, Xiao YH, et al., 2014. Fluid–structure interaction analysis by coupled FE–SPH model based on a novel searching algorithm. *Computer Methods in Applied Mechanics and Engineering*, 276:266-286. https://doi.org/10.1016/j.cma.2014.04.001

ISO (International Organization for Standardization), 1992. Quality Assurance Requirements for Measuring Equipment–Part 1: Metrological Confirmation System for Measuring Equipment, ISO 10012-1:1992. ISO, Geneva, Switzerland.

Koshizuka S, Oka Y, Tamako H, 1995. A particle method for calculating splashing of incompressible viscous fluid. Proceedings of the International Conference on

Mathematics and Computations, Reactor Physics, and Environmental Analyses, p.1514-1521.

Lauber G, Hager W, 1998. Experiments to dambreak wave: horizontal channel. *Journal of Hydraulics Research*, 36(3):291-307. https://doi.org/10.1080/00221689809498620

Liu GR, Liu MB, 2003. Smoothed Particle Hydrodynamics: a Meshfree Particle Method. World Scientific, Singapore.

Long T, Hu DA, Yang G, et al., 2016. A particle-element contact algorithm incorporated into the coupling methods of FEM-ISPH and FEM-WCSPH for FSI problems. *Ocean Engineering*, 123:154-163. https://doi.org/10.1016/j.oceaneng.2016.06.040

Long T, Hu DA, Wan DT, et al., 2017. An arbitrary boundary with ghost particles incorporated in coupled FEM–SPH model for FSI problems. *Journal of Computational Physics*, 350:166-183. https://doi.org/10.1016/j.jcp.2017.08.044

Lucy LB, 1977. A numerical approach to the testing of the fission hypothesis. *Astronomical Journal*, 82:1013-1024. https://doi.org/10.1086/112164

Monaghan JJ, 1989. On the problem of penetration in particle methods. *Journal of Computational Physics*, 82(1):1-15. https://doi.org/10.1016/0021-9991(89)90032-6

Monaghan JJ, 1992. Smoothed particle hydrodynamics. *Annual Review of Astronomy and Astrophysics*, 30:543-574. https://doi.org/10.1146/annurev.aa.30.090192.002551

Monaghan JJ, 1994. Simulating free surface flows with SPH. *Journal of Computational Physics*, 110(2):399-406. https://doi.org/10.1006/jcph.1994.1034

Newmark NM, 1959. A method of computation for structural dynamics. *Journal of the Engineering Mechanics Division*, 85(3):67-94.

Versteeg HK, Malalasekera W, 1995. An Introduction to Computational Fluid Dynamics: the Finite Volume Method. Longman, Malaysia.

Wilson EL, Farhoomand I, Bathe KJ, 1973. Nonlinear dynamic analysis for complex structures. *Earthquake Engineering and Structural Dynamics*, 1:241-252.

Yang Q, Jones V, McCue L, 2012. Free-surface flow interactions with deformable structures using an SPH–FEM model. *Ocean Engineering*, 55:136-147. https://doi.org/10.1016/j.oceaneng.2012.06.031

Zhang ZC, Qiang HF, Gao WR, 2011. Coupling of smoothed particle hydrodynamics and finite element method for impact dynamics simulation. *Engineering Structures*, 33(1):255-264. https://doi.org/10.1016/j.engstruct.2010.10.020

中文概要

题　目： 与流固耦合相关的溃坝问题中阻尼的数值及实验研究

目　的： 1. 通过全面的实验研究考察阻尼在流固耦合（FSI）问题中的影响作用；2. 提出一套光滑粒子流体动力学（SPH）和有限元方法（FEM）相结合的耦合算法，并对流固耦合系统进行数值模拟。

创新点： 1. 通过一系列实验研究惯性驱动问题中阻尼的影响并使用本文提出的数值方法进行验证；2. 该数值方法能够在不解耦的情况下对完整系统进行求解。

方　法： 1. 构建数值模型模拟流体和弹性结构之间的强烈相互作用；2. 利用 SPH 和 FEM 对流体和结构分别进行模型化；3. 采用接触力学对系统中的流固耦合机理进行建模。

结　论： 1. 基于 SPH-FEM 耦合的 FSI 模型可成功模拟自由液面形状、橡胶板的位移以及容器壁上的压强；2. 模拟结果显示，在连续相互作用的惯性驱动问题中阻尼并不是必要的考虑因素。

关键词： 阻尼；流固耦合；光滑粒子流体动力学；接触力学；溃坝问题